



## Shape of a frictional fluid finger

Eirik G. Flekkøy <sup>1,2</sup>, Bjørnar Sandnes,<sup>3</sup> and Knut Jørgen Måløy <sup>1,4,\*</sup><sup>1</sup>*PoreLab, Department of Physics, University of Oslo, NO-0316 Oslo, Norway*<sup>2</sup>*PoreLab, Department of Chemistry, Norwegian University of Science and Technology, Trondheim, Norway*<sup>3</sup>*Department of Chemical Engineering, Swansea University, Swansea, Wales SA1 8EN, United Kingdom*<sup>4</sup>*PoreLab, Department of Geoscience and Petroleum, Norwegian University of Science and Technology, Trondheim, Norway*

(Received 2 March 2023; revised 25 April 2023; accepted 28 September 2023; published 20 November 2023)

Frictional fluid dynamics describes the displacement patterns that arise when a confined mixture of liquid and grains are displaced by an immiscible fluid under pressures that are too small to cause drainage into single pores. The flow, which is governed by solid friction and capillary forces, thus bulldozes the grains into compaction fronts which give rise to propagating fingers that eventually interact to create a range of patterns, including labyrinthine ones. We derive an analytic description that successfully reproduces the experimental results for the shape of a single finger as well as the compaction front profile. The theory thus depends on only one fitting parameter.

DOI: [10.1103/PhysRevFluids.8.114302](https://doi.org/10.1103/PhysRevFluids.8.114302)

### I. INTRODUCTION

Strikingly similar labyrinthine patterns arise in highly different contexts, ranging from those of geology, physics, biology, and engineering. For instance, when a fluid displaces another containing a granular medium in a Hele-Shaw cell, the resulting frictional fluid dynamics may create labyrinthine patterns [1–6]. These patterns resemble those found on brain corals [7] as well as those found in the cross section of maxilloturbinates in seal noses [8] or the buoyancy tank of cuttlefish [9], the patterns left by magma intrusions in fractured rocks [10,11], or the structures formed by ferrofluids in a Hele-Shaw cell subject to an external magnetic field [12]. In all of these processes some principle of optimization is at work that governs the length scale and structure of the resulting patterns: in the case of frictional fluid dynamics the power is minimized by the invading fingers [3]. In the case of ferrofluids in a magnetic field, a pattern is formed that minimizes the free energy [12], while in the biological cases the patterns are understood in terms of natural evolution towards functional optimization [9,13]. The term *frictional fluid dynamics* [4] was coined to describe fluid flow governed by the combined action of pressure, capillary forces, and solid friction; a typical setup yielding such dynamics is illustrated in Fig. 1. The labyrinthine patterns resulting from such dynamics are relatively well understood at the level of the pattern length scale [3–5,14,15]. At a constant extraction rate the minimization of the power amounts to finding the finger width that minimizes the pressure needed to overcome the frictional and capillary forces. However, the smaller scale dynamics that define the actual finger shape is much less understood. The purpose of the present paper is to understand how the power minimization principle may be applied to determine the structure of the fingers, which are responsible for the emerging patterns. Finding quantitative agreement with experiments in the case of straight, steady state fingers we proceed in a

\*flekko@fys.uio.no

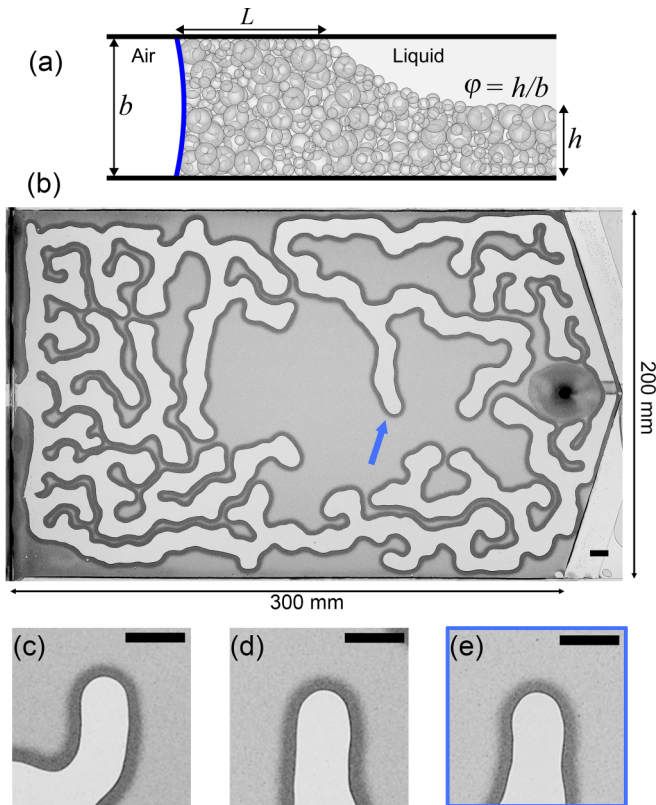


FIG. 1. (a) Sketch of a cross section through the granular front. The air-liquid meniscus (blue line) bulldozes a front of compacted grains of thickness  $L$ . The initial filling level  $\varphi$  is the ratio between the height of the initial granular layer  $h$  and the cell gap  $b$ . The pressure of the invading fluid balances the combined action of the capillary forces and the friction of the compacted front. (b) Experimental cell (horizontal) imaged from below. Liquid is slowly drained from a hole at the right hand side and air invades from the open edge on the left hand side. (c)–(e) Zoomed in view of different frictional fingers (rotated to point vertically) taken during active growth. The granular compaction front can be seen as a dark band surrounding the internal finger meniscus. The location of panel (e) is indicated with blue arrow in (b), while the (c) and (d) images are taken at other times. This experiment had  $\varphi = 0.4$ ,  $b = 0.5$  mm, fluid withdrawal rate  $Q = 0.01$  mL/min, and all scale bars are 1 cm.

more qualitative way to identify the fluctuation based mechanisms that are responsible for meandering and tip splitting.

Frictional fingers may be considered a granular analogy of the classical Saffman-Taylor finger which forms when a fluid of less viscosity displaces another at a higher viscosity in a Hele-Shaw cell [16,17], the difference being that in our case the viscous forces are replaced by solid friction. While the solution for the Saffman-Taylor finger contains the finger width as an undetermined parameter, the current solution fixes the finger width and shape via the ratio of a friction coefficient to the effective surface tension, which is a fitting parameter in the present context, but measurable.

## II. THEORETICAL DESCRIPTION

The equations that govern the shape of a displacement front are based on the concept of an effective surface tension [1]  $\gamma$  that gives rise to a capillary pressure  $\kappa\gamma$ , where  $\kappa$  is the in-plane

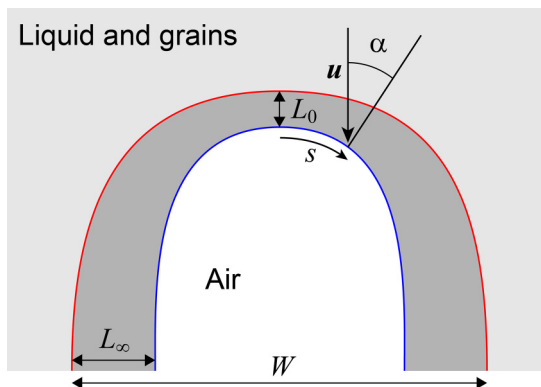


FIG. 2. Geometry of the invading air finger in the reference frame of the finger.

curvature of the air-liquid interface and a frictional pressure contribution  $\mu L$  that is linear in the thickness  $L$  of the packed front [see Fig. 1(a)] and a constant friction coefficient  $\mu$ . In Ref. [1] it is shown that the effective surface tension may be written

$$\gamma = \gamma_0(a + a_p \cos \alpha_p), \quad (1)$$

where the specific area  $a$  is the ratio of the air-liquid interface area to the total area of the granular front that is exposed to the air, while  $a_p$  is the corresponding quantity for the area that the particles expose to the air along the front,  $\gamma_0$  is the normal air-liquid surface tension, and  $\alpha_p$  is the contact angle between the air-liquid interface and the surface of the particles.

A friction law that is linear in  $L$  may arise in several ways [1]. First, it may result as a linear approximation to the exponential law that describes the effect of Coloumb friction and jamming at the front [3–5,14,15], by expanding it in small values of the Jansen coefficient that relates in plane and out of plane stresses. Second, it may become a reasonable description when the granular deformation and stretching removes sideways support for the force chains that cause jamming. In this case jamming effects disappear and the resistance to front displacement should be proportional to the number of particle contacts, i.e., to  $L$ .

Even though the fingers meander back and forth rather than keeping a straight course, and frequently come to a halt, they exhibit periods of steady motion where the tip curvature and width are approximately constant.

We therefore apply the frame of reference that follows the front tip and look for a steady state solution of the finger shape and front width. The distance along the air-grain front from the fingertip is denoted  $s$  and the angle between the velocity of the incoming grains and the front normal  $\alpha$ ; see Fig. 2.

A rectangular volume of incompressible grains in the compacted front that is stretched in one direction will contract in the other: let the normal side edges have length  $L$  and  $ds$  and the grains move along the front by a velocity  $v(s)$ . At any constant  $s$  value, the net volume flux over the side edges of length  $L$  must be balanced by a corresponding growth of  $L$ , that is, during a time  $dt$ ,  $[L(s, t + dt) - L(s, t)]ds = [L(s, t)v(s) - L(s + ds, t)v(s + ds)]dt$ . The change in  $L$  due to the accumulation of grains that arrive at a velocity  $u \cos \alpha$  is  $dL = u \cos \alpha dt \varphi / (1 - \varphi)$ . Thus the combination of stretching and grain accumulation at a front causes the finger front width  $L$  to evolve with time  $t$  according to the equation

$$\frac{\partial L}{\partial t} = -\frac{\partial(Lv)}{\partial s} + \frac{\varphi}{1 - \varphi} u \cos \alpha, \quad (2)$$

where  $\varphi$  is the solid fraction (see Fig. 1),  $u$  is the grain velocity, and  $v$  is the velocity in the direction along the front. In the laboratory frame of reference the compaction front only advances in its normal

direction and so the force on the noncompacted outside region is in this normal direction as well. Therefore, the forces only act to change the granular velocity in the normal direction and so the tangential velocity is conserved. In the finger frame of reference this implies that  $v = u \sin \alpha$ . Our main approximation is to assume that  $\alpha$  describes the orientation both of the inner and outer part of the compacted front—an approximation that is expected to break down at high  $\varphi$  values when the front becomes thick.

The local curvature

$$\kappa = \frac{\partial \alpha}{\partial s} \quad (3)$$

determines the capillary pressure  $\gamma\kappa$ , which together with the linear frictional pressure  $\mu L$  gives the total pressure drop

$$\Delta P = \mu L + \gamma\kappa \quad (4)$$

over the front. Note that, in addition to the capillary pressure  $\gamma\kappa$ , which is due to the in-plane curvature, there is also the capillary pressure  $\Delta P_w = 2\gamma_0 \cos \alpha_w / b$ , where  $b$  is the plate separation and  $\alpha_w$  the contact angle at the plates. This pressure is due to the out-of-plane curvature, and typically  $\Delta P_w > \gamma\kappa$ , but since  $\Delta P_w$  is constant all along the finger front, it only amounts to a fixed addition in the pressure drop and will therefore be ignored.

Using the derivative relation  $\partial/\partial s = (\partial\alpha/\partial s)\partial/\partial\alpha = \kappa\partial/\partial\alpha$  the steady state form of Eq. (2) becomes

$$\frac{\partial L}{\partial s} = \left( \frac{\varphi}{1-\varphi} - \kappa L \right) \cotan \alpha, \quad (5)$$

where  $u$  has canceled out.

Along the straight parts of the finger the curvature  $\kappa = 0$  and  $L = L_\infty$ , so that  $\Delta P = \mu L_\infty$ , which allows us to write Eq. (4) as

$$\kappa = \frac{\Delta P - \mu L}{\gamma} = \frac{\mu(L_\infty - L)}{\gamma}, \quad (6)$$

which when inserted in Eq. (5) yields

$$\frac{\partial L}{\partial s} = \left( \frac{\varphi}{1-\varphi} - \frac{\mu}{\gamma}(L_\infty - L)L \right) \cotan \alpha. \quad (7)$$

Since  $\cotan \alpha$  diverges at the fingertip where  $\alpha = 0$ , the term in the parentheses must vanish in order to yield a finite solution for  $L$ . Setting this prefactor to zero and solving for  $L_\infty$  yields

$$L_\infty = L_0 + \frac{\gamma\varphi}{\mu L_0(1-\varphi)} \quad (8)$$

at  $s = 0$  where  $L = L_0$ .

The principle of minimum power at a constant air injection rate amounts to a requirement of minimum pressure. In other words, the fingers must have a width  $W$  that minimizes  $\Delta P = \mu L_\infty$ . Since the width  $W = 2L_\infty/\varphi$  by mass conservation and  $L_\infty$  is a function only of  $L_0$  (taking  $\varphi$ ,  $\gamma$ , and  $\mu$  to be constants) this means that  $\partial L_\infty/\partial L_0 = 0$ . Doing the derivative and solving this equation for  $L_0$  gives the front tip width

$$L_0 = \sqrt{\frac{\gamma\varphi}{\mu(1-\varphi)}} = \frac{L_\infty}{2} \quad (9)$$

by use of Eq. (8).

The  $L_\infty = 2L_0$  relationship is a result of the linear friction law in Eq. (4). In the more general case where an arbitrary friction law is assumed by replacing  $\mu L \rightarrow \mu(L)L$  in Eq. (4), Eq. (8) would

be replaced by

$$\mu(L_\infty)L_\infty - \mu(L_0)L_0 = \gamma \frac{\varphi}{L_0(1-\varphi)}, \quad (10)$$

which in general would not give  $L_\infty = 2L_0$ . However, the right hand side of Eq. (10) is the capillary pressure contribution at the tip and so corresponds to a tip curvature

$$\kappa_0 = \frac{\varphi}{L_0(1-\varphi)}, \quad (11)$$

which is independent of the particular friction law that is assumed. In other words, any nonlinear friction law will give rise to the same relationship between the tip curvature and front thickness. This relationship is governed by the balance of front stretching and accumulation alone. In Ref. [1] we assumed the front profile to be circular with a constant curvature  $\kappa_0$  (resulting in a discontinuity at the point where the curved front connects with the straight side segments) and to have a constant width  $L_0$ . These assumptions yield the same curvature as in Eq. (11).

Returning to the linear friction law, using Eq. (9), and introducing  $\Delta L = L - L_0$ , Eq. (5) may be written

$$\frac{\partial \Delta L}{\partial s} = \frac{\mu \Delta L^2}{\gamma} \cotan \alpha \quad (12)$$

and, from Eqs. (3), (6), and (9), the equation for  $\alpha$

$$\frac{\partial \alpha}{\partial s} = \frac{\mu(L_0 - \Delta L)}{\gamma}, \quad (13)$$

with the boundary conditions  $\alpha(0) = 0$  and  $\Delta L(0) = 0$ .

In the small  $s$  limit where  $\cotan \alpha \approx 1/\alpha$  these equations are easily solved to yield  $\alpha = \mu L_0 s / \gamma$  and

$$\Delta L = \frac{L_0}{L_0 / \Delta L_0 - \ln(s/s_0)}, \quad (14)$$

where  $\Delta L_0$  is the value at some other  $s_0 \ll \gamma / (\mu L_0)$ . The divergence of the derivative of  $\Delta L(s)$  implies a cusp at the fingertip, which is an unphysical result of the assumption that  $\alpha$  describes the outer as well as the inner boundary of the compaction front. By a refined geometric treatment of the outer boundary orientation, including its dependence on  $\partial L / \partial s$ , it may be shown that  $\Delta L \propto s^2$  near the tip. However, as this treatment too relies on a small  $\varphi$  approximation, we will stay with the original and simpler approximation.

Introducing the dimensionless quantity  $s' = \mu L_0 s / \gamma$  and  $\Delta L' = \Delta L(s') / L_0$  all dimensional quantities drop out in Eq. (12) and Eq. (13). The physical coordinates of the air interface  $\mathbf{x}(s)$  may also be nondimensionalized into  $\mathbf{x}'(s') = \mu L_0 \mathbf{x}(s) / \gamma$  and likewise for the outer front boundary  $\mathbf{x}'_{\text{out}}(s')$ , yielding the functional forms

$$\mathbf{x} = \frac{\gamma}{\mu L_0} \mathbf{x}'(s'), \quad (15)$$

while the outer perimeter of the compacted region is given by

$$\mathbf{x}^{\text{out}} = \mathbf{x} + \mathbf{n}, \quad L = \frac{\gamma}{\mu L_0} \mathbf{x}'(s') + L_0 \mathbf{n} [1 + \Delta L'(s')], \quad (16)$$

where  $\mathbf{n}$  is the outwards unit normal and  $s'$  may now be taken as an arbitrary parametrization of the curve. Here the curves  $\mathbf{x}'(s')$  and  $\Delta L'(s')$  are independent of  $\mu$ ,  $\gamma$ , and  $\varphi$ .

The numerical integration of Eq. (12) and Eq. (13) is straightforward and relies on the centered difference approximation of the derivatives. It starts from an initial point, where  $\alpha \approx \pi/2$  and  $\Delta L = L_0$ , that is at a straight segment of the front. Figure 3 shows the details of the logarithmic singularity

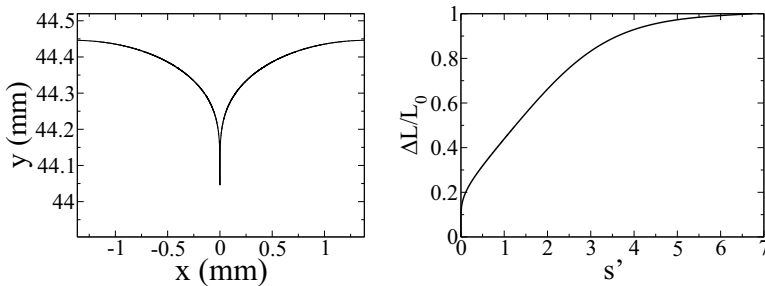


FIG. 3. Closeup of the finger shape at the tip and the relative increment in the front width  $\Delta L/L_0$  as a function of the dimensionless  $s' = sL_0\mu/\gamma$  when  $\varphi = 0.4$ .

of the front and how  $\Delta L$  varies with the length from the tip along the air-grain interface. Note that the singular behavior is expressed as a steep drop where  $\Delta L$  varies only  $\sim 20\%$  of  $L_0$ .

### III. COMPARISON WITH EXPERIMENTS

The experimental setup, which is illustrated in Fig. 1, is described in Ref. [4]. A Hele-Shaw channel with cell gap  $b = 0.5$  mm is loaded with a 50% (by volume) mixture of water and glycerol containing suspended polydisperse glass beads of mean diameter  $75 \mu\text{m}$  [5]. The grains settle after loading and form a layer of thickness  $h$  on the bottom plate (Fig. 1) such that the initial filling level  $\varphi = h/b$ . The liquid is subsequently withdrawn using a syringe pump (Harvard Scientific, PHD Ultra) at controlled withdrawal rate  $Q = 0.01$  mL/min, which is set sufficiently low that viscous forces can be neglected. A hole in the top plate is used for both the initial loading and the fluid withdrawal. As the cell is slowly drained air at atmospheric pressure invades from the open edge [left hand side in Fig. 1(b)] and eventually forms the labyrinthine pattern of frictional fingers as shown in Fig. 1(b) ( $\sim 20$  h after the start of the experiment). Individual fingers are cropped from the images during phases of near steady state growth. Examples are shown in Figs. 1(c)–1(e). The cropped images of individual fingers were then rotated and aligned before the  $x$  and  $x_{\text{out}}$  curves were identified manually by selecting the locations along the front of maximum grayscale contrast.

Mass conservation relates the width  $W$  of the fingers to the front width  $L_\infty = 2L_0$  so that Eq. (9) may be used to set  $\gamma/\mu = W^2\varphi(1-\varphi)/16$  for each experiment by measurement of the average  $W$ . This is the only parameter that is fitted to the experiments. The packing fraction  $\varphi$  was measured prior to the injection of the fluid grain mixture. In Fig. 4, which shows a comparison between theory and experiments for  $\varphi = 0.23$  and  $0.4$ , good agreement is observed. For larger  $\varphi$  values the tip growth happens without the steady sequences where the tip curvature/width remains constant. Instead the tips typically start out pointed and evolve to a blunted shape via sideways bulging.

As a consistency check it is interesting to use the experimental  $W$  values to estimate the relative magnitude of the forces at play. Since  $L_0 = L_\infty/2$  the capillary pressure at the fingertip  $\gamma\kappa_0 = \mu(L_\infty - L_0) = \mu L_0$ , so that the frictional and capillary forces have the same order of magnitude. Taking the last factor of Eq. (1) to be unity  $\gamma \approx \gamma_0 \approx 0.05$  N/m, the air water/glycerol surface tension. Figures 4 indicate a radius of curvature  $1/\kappa_0 \approx 5$  mm, so that the capillary and frictional pressures are both  $\sim 10$  Pa.

The experiments show a slightly blunter shape than what is predicted from the assumption of a steady state force balance along the front. This effect is likely caused by the fluctuations in packing density and granular structure along with fluctuations in the frictional force, both of which have been ignored up to this point. Fluctuations in the packing density will cause fluctuations in  $L$  according to Eq. (2), where it should be noted that the last term that describes accumulation goes as  $u \cos \alpha$ .

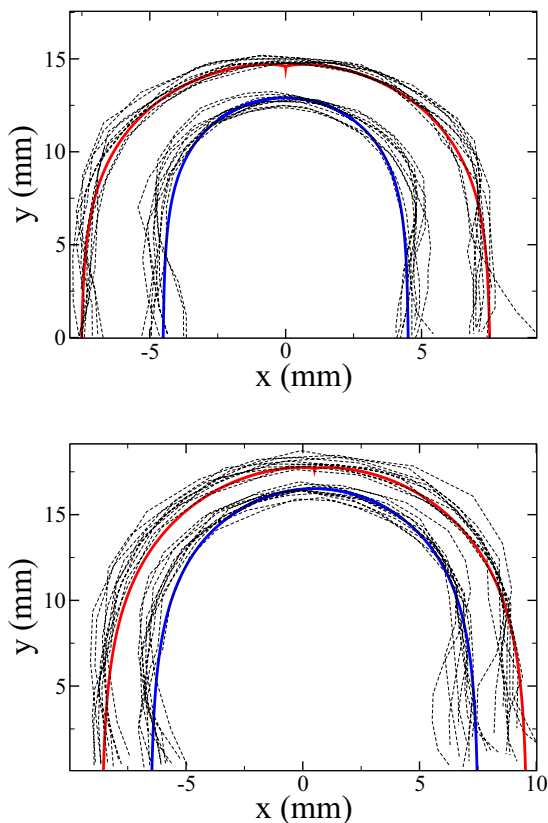


FIG. 4. Finger shapes for  $\varphi = 0.4$  (top figure) and  $\varphi = 0.23$  (lower figure). The theory of Eqs. (15) and (16) is shown by the full red curves and experiments by stapled lines. The experimental fingers are all recorded while moving.

This means that such fluctuations are more frequent at the tip. In addition, any velocity dependence in  $\mu$  will cause the largest pressure fluctuations at the tip where this velocity is largest. Thus the fluctuations in the threshold stress required for front motion will both be larger and more frequent at the tips. For this reason the front is more likely to stop its motion right at the tip, rather than on the sides. Figure 5 shows how these effects lead to a blunting of the fingertips in the stopping process. These mechanisms may also cause tip splitting in those cases where the bulging is not stopped by friction, but continues as a new finger, as is often observed.

In conclusion, we have developed a simple analytic description of the frictional fluid finger evolution. The agreement with experiments suggests that the finger width and structure are those which minimize the power needed to form them as a balance is established between the pressure in the invading fluid, capillary, and frictional forces. Compared to the Saffman-Taylor fingers, which result from long range viscous forces, the frictional fluid fingers represent a distinct hydrodynamic phenomenon that is entirely governed by short range forces.

#### ACKNOWLEDGMENT

This work was partly supported by the Research Council of Norway through its Centers of Excellence funding scheme, Project No. 262644, and the Engineering and Physical Sciences Research Council, Project No. EP/S034587/1.

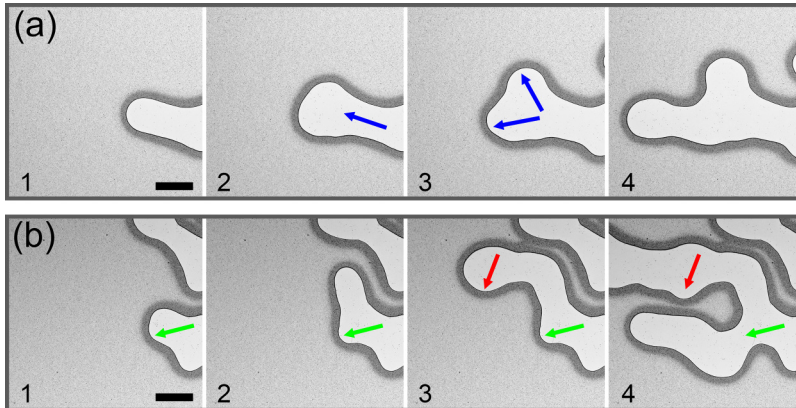


FIG. 5. (a) Snapshots of an advancing finger (frame 1) that takes on a bulbous shape as the growth comes to a halt (blue arrow, frame 2). Tip splitting (frame 3) causes a branching into two fingers (frame 4). (b) The side bulge indicated by the green arrow remains static for a while, but eventually side branches to form a new finger. The red arrow illustrates a bulge that will remain static as growth is blocked by a neighboring finger. Scale bar: 1 cm.

- 
- [1] H. A. Knudsen, B. Sandnes, E. G. Flekkøy, and K. J. Måløy, Granular labyrinth structures in confined geometries, *Phys. Rev. E* **77**, 021301 (2008).
- [2] J. Eriksen, R. Toussaint, K. Måløy, E. Flekkøy, and B. Sandnes, Numerical approach to frictional fingers, *Phys. Rev. E* **92**, 032203 (2015).
- [3] B. Sandnes, H. A. Knudsen, K. J. Måløy, and E. G. Flekkøy, Labyrinth patterns in confined granular-fluid systems, *Phys. Rev. Lett.* **99**, 038001 (2007).
- [4] B. Sandnes, E. G. Flekkøy, H. A. Knudsen, K. J. Måløy, and H. See, Patterns and flow in frictional fluid dynamics, *Nat. Commun.* **2**, 288 (2011).
- [5] J. A. Eriksen, R. Toussaint, K. J. Måløy, E. Flekkøy, O. Galland, and B. Sandnes, Pattern formation of frictional fingers in a gravitational potential, *Phys. Rev. Fluids* **3**, 013801 (2018).
- [6] C. Chevalier, A. Lindner, and E. Clément, Destabilization of a Saffman-Taylor fingerlike pattern in a granular suspension, *Phys. Rev. Lett.* **99**, 174501 (2007).
- [7] S. Lin, N. Chou, D. Bao, G. Zhang, C. Xiong, J. Fang, and Y. M. Xie, Design and fabrication of artificial brain coral: Evolution principle, turbulent hydrodynamics and matter interchange, *Comput. Struct.* **276**, 106955 (2023).
- [8] M. Mason, L. Wenger, Ø. Hammer, and A. Blix, Structure and function of respiratory turbinates in phocid seals, *Polar Biol.* **43**, 157 (2020).
- [9] T. Yang, Z. Jia, H. Chen, Z. Deng, W. Liu, L. Chen, and L. Li, Mechanical design of the highly porous cuttlebone: A bioceramic hard buoyancy tank for cuttlefish, *Proc. Natl. Acad. Sci. USA* **117**, 23450 (2020).
- [10] G. Baer and Z. Reches, Mechanics of emplacement and tectonic implications of the ramon dike systems, israel, *J. Geophys. Res.* **96**, 11895 (1991).
- [11] K. V. Cashman, R. S. J. Sparks, and J. D. Blundy, Vertically extensive and unstable magmatic systems: A unified view of igneous processes, *Science* **355**, eaag3055 (2017).
- [12] S. A. Langer, R. E. Goldstein, and D. P. Jackson, Dynamics of labyrinthine pattern formation in magnetic fluids, *Phys. Rev. A* **46**, 4894 (1992).
- [13] E. G. Flekkøy, L. P. Folkow, S. Kjelstrup, M. J. Mason, and Ø. Wilhelmsen, Thermal modeling of the respiratory turbinates in arctic and subtropical seals, *J. Thermal Biol.* **112**, 103402 (2023).



- [14] R. Holtzman, M. L. Szulcowski, and R. Juanes, Capillary fracturing in granular media, [Phys. Rev. Lett. \*\*108\*\*, 264504 \(2012\)](#).
- [15] Y. Meng, B. K. Primkulov, Z. Yang, C. Y. Kwok, and R. Juanes, Jamming transition and emergence of fracturing in wet granular media, [Phys. Rev. Res. \*\*2\*\*, 022012\(R\) \(2020\)](#).
- [16] R. Combescot, T. Dombre, V. Hakim, Y. Pomeau, and A. Pumir, Shape selection of Saffman-Taylor fingers, [Phys. Rev. Lett. \*\*56\*\*, 2036 \(1986\)](#).
- [17] P. Saffmann and G. Taylor, The penetration of a fluid into a porous medium or hele-shaw cell containing a more viscous liquid, [Proc. R. Soc. London A \*\*245\*\*, 312 \(1958\)](#).